Plasma Physics and Controlled Fusion

Halides formation dynamics in nanosecond and femtosecond laser induced breakdown spectroscopy

To cite this article before publication: Nerea Bordel *et al* 2022 *Plasma Phys. Control. Fusion* in press https://doi.org/10.1088/1361-6587/ac5c11

IOP Publishing Plasma Physics and Controlled Fusion
Plasma Phys. Control. Fusion **XX** (XXXX) XXXXXX https://doi.org/XXXX/XXXX

Halides formation dynamics in nanosecond and femtosecond laser induced breakdown spectroscopy

N. Bordel[1], L.J. Fernández-Menéndez[1], C. Méndez-López[1], C. González-Gago[1] and J. Pisonero[1]
[1] Department of Physics, University of Oviedo, Federico García Lorca 18, 33007 Oviedo, Spain
Email:
bordel@uniovi.es

Received xxxxxx
Accepted for publication xxxxxx
Published xxxxxx

Abstract

LIBS is an analytical technique based on the measurement of the emitted radiation coming from a laser-induced plasma (LIP) created after irradiation of a sample by a short duration laser pulse. Research about molecular presence in LIPs has increased because the use of molecular emission has proven an encouraging way to improve LIBS abilities. LIPs are dynamic plasmas with fast time and spatial evolutions, in which atoms and molecules can follow different paths in their evolution and distribution. Molecular creation mechanisms within LIPs are still a challenging issue under investigation and the prevalence of some specific mechanisms are dependant on experimental conditions (sample nature, laser parameters, surrounding atmosphere…). In this work, different time and spatially solved experiments were carried out in ns- and fs-LIBS to investigate the dynamics of alkaline-earth (Ca) halide (F) diatomic molecule formation. Experiments were carried out on powdered CaF_2 samples for both ns- and fs-LIBS. The effects of a gas flow (air, He, Ar) over the plume are investigated for ns-LIBS. Nebulization-modified ns-LIBS experiments in which the alkaline-earth element is externally added to the plasma plume as an aerosol were carried out on $(C_2F_4)_n$ samples. The spatial separation between atomic and molecular emission distribution was found to take place with and without external modifications over the ns-LIP. Behaviour in fs-LIPs was determined to differ significantly from analogous experiments with nanosecond lasers, but temporal optimization remains the optimum method for molecular detection as spatial separation was not found to provide any remarkable advantage.

Keywords: laser-induced plasma, molecular emission, atomic emission, nanosecond laser, femtosecond laser, nebulization

1. Introduction

Laser-induced breakdown spectroscopy (LIBS) is an analytical technique based on the spectral analysis of the emission from a laser induced plasma (LIP). LIBS allows a fast analysis with none or minimal sample preparation, providing multi-elemental qualitative and quantitative information with spatial resolution, either in laboratory or in-situ using portable devices or remote detection systems [1,2]. These advantegous characteristics and its great versatility have motivated the increasig usage in numerous applications such as coal analysis [3] metallurgical analysis [4], environmental monitoring [5], food analysis [6], archaeology [7,8], biomedical analysis [9], or space exploration [10].

In LIBS, a high intensity pulsed laser with short pulse duration (e.g. ns or fs) is focused on a spot of the sample

surface, which absorbs the radiation, and the ablation of a small volume of matter is produced. The mechanism of ablation differs significantly according to the pulse duration [11]. For a ns-laser, which conforms the usual LIBS set-ups, ablation is the result of mainly thermal vaporization. Afterwards, the vaporized matter interacts with the on-going laser pulse, getting furtherly heated and excited/ionized. Free electrons experience inverse Bremsstrahlung processes and, ultimately, a dense plasma is produced, partially shielding the surface from laser irradiation. This plasma-laser interaction results in an ionized and excited transient plasma that decays in the span of several tens of microseconds, depending on the laser parameters. The stages that characterize the ns-LIP evolution involve an early continuum emission due to free-bound and free-free transitions, followed by the population of high-energy levels of mainly ionic species. Afterwards, the presence of transitions involving lower upper-level energies of ions and atomic species is observed and, eventually, excited molecules formed by recombination dominate the spectral emission [12].

Femtosecond lasers, which are increasingly used in LIBS [13], present fundamental differences in the ablation process with respect to common ns-lasers, as well as lack of laser-plasma interaction [14, 15]. The much higher irradiance produces ionizations on the sample, which translate into Coulomb explosions produced by the repulsion of closely and densely located ions. Additionally, the short laser pulse duration results in no thermal damage effects observed on the sample. The fs-laser pulse ends before any laser-plasma interaction can take place; therefore, the fs-laser induced plasma (fs-LIP) is characterized by lower excitation temperatures and a significant presence of neutral atoms in the fundamental state, as well as a much faster decay (few microseconds). The fs-LIP evolution involves much lower continuum emission and the early (tens of nanoseconds) presence of atomic and molecular emission, some of which correspond to molecules native to the sample, whose bonds were not broken in the ablation process [16-18].

Nevertheless, halogen resonant emission lines are in the vacuum ultraviolet spectral region [19] so they are not a suitable choice of analytical lines for LIBS applications. To overcome this drawback the usual procedure consists in the use of the atomic emission from transitions with lower levels in the first excited multiplet and whose wavelengths are in the infrared region of the spectrum. This emission is lower but can be enhanced by enriching the surrounding atmosphere with He, either by introducing the sample in a controlled-atmosphere chamber [20] or by directing a He gas flow [21] onto the laser incidence spot.

Alternatively, halogens presence in the plasma can also be determined by detecting the molecular emission of halogen-containing diatomic molecules. Particularly, it was observed that halogens easily recombine with alkali-earths (e.g. Ca, Sr) forming molecules whose emission can be measured under ambient conditions with much higher sensitivity than that of the atomic lines [22-23]. The detection of these molecules is also possible for alkali-earth-free samples by externally adding the alkaline earth species during the sample ablation process. In this sense, a procedure based on the nebulization of an aqueous Ca-containing solution was found suitable for the determination of F in Ca-free samples, obtaining a linear relationship between the sample F content and the detected molecular emission [24]. Nevertheless, it was also observed that the nebulization affects the plasma properties. The effects observed for a Cu model sample include changes such as higher total intensity, a diminish of electron temperatures, an enlarged plasma plume and an increase of shape instability at delay times longer than about 8 μs after the laser shot [25].

However, even if molecular emission is nowadays stablished as a good alternative for the determination of halogens, knowledge regarding the spatial and temporal distribution of the molecular species in the plasma, which is essential to optimize detection, is still scarce. Previous studies on the dynamics of molecular emission have shown that, even when nanosecond lasers are used, molecular emission occurs at delay times lower than a microsecond, although at short delay times it is significantly masked by the intense atomic emission [26]. In particular, a study carried out with spatial and temporal resolution using CaF_2 powder as model sample revealed significant differences in the temporal evolution and spatial distribution between molecular (CaF) and atomic species (Ca) [27]. This study, which used a ns-laser and was performed under regular atmospheric conditions, concluded that molecular emission maximized at delay times of around 7 – 10 μs, with a spatial distribution closer to the sample surface than that of the atomic one. This separation was maintained until delay times of the order of 45 microseconds when the molecular emission began to expand to higher heights and the atomic emission became negligible. Hence restricting the detection to the lower spatial region while mantaining a short delay (5 μs) was shown to provide a high molecular signal without strong atomic interferences [27].

All these results cannot be generalized to any LIBS set-up since there are many experimental parameters that can affect the plasma dynamics and the spatial distribution of the species. For instance, plasma dynamics could be affected by the gas environment. It is known that the use of He or Ar atmospheres give rise to changes in the atomic emission intensity, electron densities and excitation temperatures [19, 28-30]. In addition, the different thermal conductivity of the gas can modify the cool down and expansion processes of the plasma [31], producing, in turn, variations in the molecular formation, evolution, and spatial distribution which could affect LIBS capabilities for halogen-based molecular detection.

In this context, the present work thoroughly evaluates the influence of different parameters such as the atmosphere in

which the plasma is formed, the external supply of Ca to a F-containing sample or the laser pulse duration (ns or fs) on the CaF spatiotemporal evolution. In particular, the dynamics of atomic and molecular emission are studied in air, He and Ar enriched atomspheres, respectively.

2. Experimental

2.1 Nanosecond LIBS setup

A Q-Switched Nd:YAG laser (EKSPLA, NL301HT) at its fundamental wavelength (1064 nm), operating at 10 Hz, was used as excitation source. The laser beam was focused on the sample surface using a 35 mm focal length objective (Thorlabs, LMH-5X-1064), while energy was fixed at 100 mJ/pulse by means of an LOTIS-TII attenuator. The sample position was controlled by a X-Y stage comprising two stepper motors (PImiCos GmbH VT_80200-2SM and a customized linear stage). Plasma emission light was collected by a system of two plano-convex lenses with a 50.8 mm diameter, imaging it on the spectrograph entrance slit plane. The first lens (Thorlabs, LA4904-UV) has a focal length of 150 mm and the second one (Thorlabs, LA4855-UV) has a focal length of 300 mm, thus achieving a 2:1 magnification of the object. The detection system is made up by a Czerny-Turner 500 mm focal length spectrograph (Andor Technology, Shamrock SR-500i-D1) coupled to an ICCD (Andor Technology, iStar DH734-25F-03), whose matrix has 1024 x 1024 pixels (with an effective pixel size of 19.5 x 19.5 µm). A diffraction grating of 1200 lines/mm was used for this work, allowing for a 35 nm wide spectral window.

The imaging performance of this experimental set-up was calibrated by means of a resolution test target 1951 USAF (Thorlabs, R3L3S1N), which was placed in the position of the sample. The test target was illuminated from the back in such a way that its image was formed at the completely opened spectrograph slit entrance. This image was projected onto the CCD using the zero-order configuration of the diffraction grating, allowing for a straightforward experimental measurement of the resolving power which was found to be 16 line pairs per mm, corresponding to the largest set with non-distinguishable horizontal lines (element 1 of group 4) of the test target. The scale of the images was calculated to be 9.6 ± 0.3 µm/pixel. For the spatially resolved spectral measurements, the plasma image is formed at the entrance of the spectrograph making the vertical symmetry axis of the plasma match the slit (fixed at a 100 µm width), as can be seen in Figure 1. Considering the scale obtained by the test target, and identifying the row corresponding to the height on which the sample surface was placed, each row of the CCD was then associated with a plasma height.

2.1.1 Gas and aerosol inlet performance. The design of the experimental system for the gas or aerosol inlet was made under the premise of simplicity since it was intended that the halogen determination could eventually be carried out on-site with portable equipment. This, for instance, prevents the sample from being placed in vacuum chambers or controlled atmospheres. The influence of noble gases in the plasma environment was studied and contrasted with the results obtained in air, which was also blown in order to make the experimental conditions comparable. Gas blowing was performed by means of a plastic tube of 4 mm diameter, which was placed 1 cm above the sample pointing to the ablation spot, forming an angle of 50° with respect to the surface (Fig. 1). The flow control at 1.8 L/min was carried out by a mass flow controller (MKS Instruments) for noble gases injection, while for the air flow it was performed by a compressor.

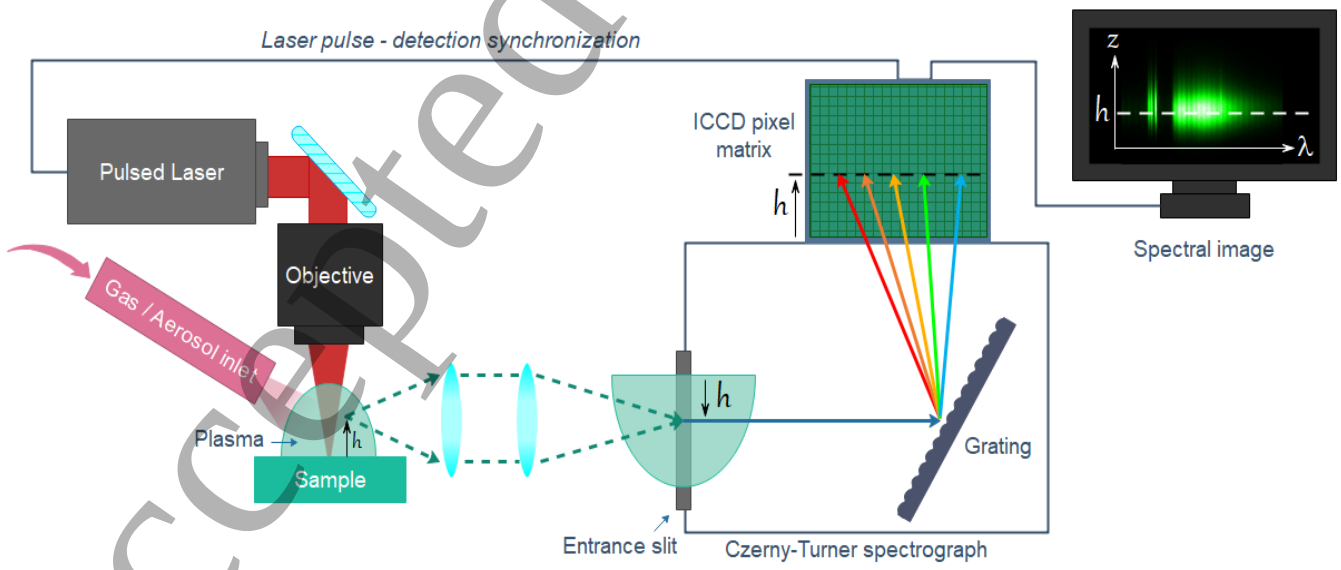

Figure 1. Schematic representation of the experimental LIBS setup.

In addition, the emission dynamics were also studied when the plasma was generated in the presence of Ca-rich aerosol. In this case, the plastic tube was replaced by a microflow concentric nebulizer (Teledyne CETAC Technologies). A 15% w/w aqueous calcium nitrite solution (Sigma Aldrich) was used as nebulized aerosol, which was introduced using a syringe pump (Thermo Fisher Scientific) at a rate of 0.24 mL/h using Ar as gas carrier, with a flow rate set to 1 L/min by the MKS mass flow controller.

2.1.2 Samples. CaF_2 (Alfa Aesar, [CaF_2] > 99.5 %) samples were used for the gas flow study, all of them properly mixed in an agate mortar. For each sample, an amount of 0.3 g of powder was homogeneously deposited on a double-sided tape fixed over a microscope slide, which was placed and horizontally levelled over the X-Y stage. For the nebulization study, Ca-free samples were required, so flat pieces of high purity polytetrafluoroethylene (PTFE) (Transglass, PPTFEA002) were used.

2.1.3 Acquisition conditions. For the gas flow study, each sample was analyzed in raster mode (spot diameter at 400 µm, laser frequency at 10 Hz and sample translation at a speed of 4 mm/s) resulting in single shot ablation at each sample site. Spectra were collected at different delay times (t_d) from 0.4 µs to 90 µs. Initially, spectra were collected every 0.2 µs since a fast plasma evolution takes place at short delay times after the laser shot; however, this integration time was progressively increased at longer delay times. Table 1 lists the experimental acquisition conditions used at the different delay times. Moreover, a correlation factor was calculated to apply for spectra collected at 15 µs and at 40 µs, in order to compare the intensities for this delay time with the results obtained for the previous acquisition conditions.

Table 1. Delay time, delay time step and gate width used for each delay range within gas flux study.

Delay time range (µs)	Time step (µs)	Gate width (µs)
0.4 – 3	0.2	0.2
3 – 5	1	0.2
7	–	0.2
10 – 15	5	0.2
15 – 40	5	2
40 – 60	5	5
60 – 90	15	5

The gain of the ICCD was fixed for all the measurements in such a way that the linear range of the CCD was never exceeded. The outcoming spectra were acquired through 4 software accumulations, where each accumulation comprised the acquisition of 12 successive plasma generated spectra (one per laser shot), accumulated on the CCD chip. Experimental data showed throughout this work were obtained by triplicating the experiments.

The nebulization study was performed in a similar way to the gas flow study, changing the acquisition times (see Table 2) in order to obtain an appropriate signal, since the ablation conditions were changed. The outcoming spectra were acquired through 3 software accumulations, where each accumulation involves the acquisition of 10 successive plasma generated spectra. All 30 plasmas were induced on the same spot. For each acquisition condition, a quadruplicate was carried out.

Table 2. Delay time, delay time step and gate width used for each delay range within Ca nebulization study.

Delay time range (µs)	Time step (µs)	Gate width (µs)
0.4 – 2.8	0.2	0.2
3 – 9.5	0.5	0.5
10 – 24	1	1
25 – 45	5	5
50 – 70	10	10

2.2 Femtosecond LIBS setup

The experimental setup includes a Yb:KGW fs-laser (Pharos, Light Conversion) integrated inside a modified ablation unit, which is part of an ablation system for LA-ICP-MS experiments (NWRFemto UltraCompact; ESI, New Wave Research Division) and fixed to an optical table (RP Reliance, Newport). The laser beam can be extracted out of the ablation chamber and is redirected by a set of custom mirrors (CVI Optics) towards a focusing objective (35 mm focal length, model LMH-5X-1064 from Thorlabs), achieving a spot diameter of approximately 60 µm. Although the experimental system is different from the one used for the nanosecond laser study, Figure 1 also provides a representative schematic example for the femtosecond study. For the purposes of the present work, the laser wavelength was the fundamental 1028 nm, and the frequency was set at 10 Hz according to experimental needs; the maximum 1.2 mJ/pulse energy was used throughout this work.

In the detection system, light from the plasma plume is directly focused onto a high-resolution spectrometer (Andor Technology, Shamrock SR-500i-D1) coupled to an ICCD (Andor Technology, iStar DH334T-18F-E3, with an effective pixel size of 13 x 13 µm) via two Ø50.8 mm plano-convex lenses of 100 and 300 mm focal lengths (LA4545-UV and LA4855-UV from Thorlabs, respectively) that result in a 3:1 magnification of the image, that was preferred due to the smaller size of fs-LIPs. The lenses are mounted on a motorized linear stage (Dover Motion) with motion parallel to the

spectrometer. The focusing distance is measured with an optoNCDT 1420 laser-meter from Micro-Epsilon. Sample positioning is controlled with a motorized stage (Dover Motion) on the XY plane and with a vertical translation stage (MVS010/M, Thorlabs) on the Z plane.

A 1200 lines/mm was also utilized for this experiment, but the spectral window was approximately 19.5 nm wide due to the smaller pixel size of the ICCD.

The imaging performance of this experimental set-up was calibrated as previously described for the nanosecond LIBS setup, obtaining a resolving power of 32 line pairs per mm, since element 1 of group 5 from the resolution target was the largest set with non-distinguishable horizontal lines. The scale of the images was calculated to be 4.25 ± 0.08 μm/pixel.

The samples used in this section were the same as those used for the gas flow study (CaF_2 powder).

2.2.1 Acquisition conditions. A quadruplicate of the measurements was carried out, accumulating a total of 100 spectra in each case (10 chip accumulations x 10 software accumulations, aiming to reduce reading noise) while simultaneously moving the sample at 3.16 mm/s to have a fresh powder surface at each spot. Each raster line had a length of 31.6 mm and lines were separated by roughly half a millimeter. Acquisition times are shown in Table 3.

Table 3. Delay time, delay time step and gate width used for each delay range within femtosecond laser study.

Delay time range (μs)	Time step (μs)	Gate width (μs)
0.05 – 0.50	0.05	0.05
0.6 – 1.0	0.1	0.1
1.5 – 5.0	0.5	0.5
6 – 10	1	1

3. Results

In all three studies, spectral emissions from the atomic (Ca) and molecular (CaF) species which populate the plasma were acquired with spatial and temporal resolution. The analysis of the atomic emission behavior was carried out integrating the intensity of Ca I emission lines at 526.18, 526.58 and 527.03 nm as function of time and height in the plasma plume, while for the molecular emission characterization the sequence $\Delta v=0$ of the $B^2\Sigma \rightarrow X^2\Sigma$ system (529.00-538.00 nm) was used. Specifically, wavelengths from 529.00 to 534 nm and from 536 to 538 nm were considered for molecular emission integration, in order to avoid the interference of the Ca I line at 534.5 nm [32, 33]. The diffraction grating was centered at 533.00 nm, which enabled to record Ca and CaF at the same spectral image, significantly reducing the uncertainty in the correlation of their respective emission behaviour.

3.1 Effect of the flowing gas

As indicated in the introduction, several parameters can influence the behaviour of atomic and molecular emission in a laser induced plasma. Among those parameters the atmosphere in which the plasma is produced can play a key role. To explore the effect of the nature of the surrounding gas, experiments using Ar and He gas flow were carried out. As a previous step, it was necessary to confirm that the presence of a flowing gas was not influencing the results. For this purpose, new experiments maintaining the air environment were carried out reproducing those described in [27] but, in these new experiments air was flowing close to the sample in the same way than He or Ar. The experiments with flowing air provided similar results to those seen in [27] with no air flow, showing that the gas flow was not producing significant alterations on the plasma dynamics and emission spatial distribution. Therefore, as the rest of the experimental conditions were mantained (ns-laser setup, sample condition and acquisition times, etc.) it can be stated that the observed differences when flowing Ar or He would be caused by the gas nature and not by the gas flow.

Figure 2 shows the spectral image obtained from the central, normal axis of the plasma with the three different flowing gases (emission signals were normalized at each represented image). Spectra corresponding to a 5 μs delay time evolution stage of the plasma are presented as a representative time in which clear differences due to the flown gases become apparent.

As already found in [27], the plasma generated in air results in a spatial separation between the atomic and molecular emitters at short delay times (< 45 μs); in particular, Figure 2(a) shows an atomic emission expansion of 2 mm in height while the molecular one does not exceed 0.5 mm. However, as can be seen in Figure 2(b), there is no significant spatial separation between the atomic and molecular radiation when Ar is used, since the areas of predominance of both emissions are at the same height (although maximum molecular intensity is much lower than the atomic one). The plasma formed in a He-rich environment (Figure 2(c)) shows a pronounced expansion reaching almost 4 mm in height. However, while the atomic emission shows high intensity in a broad range of heights, the region where the highest molecular emission occurs is located at distances from the sample surface lower than 1 mm. In addition, a second region with low molecular emission takes place between 2 and 4 mm.

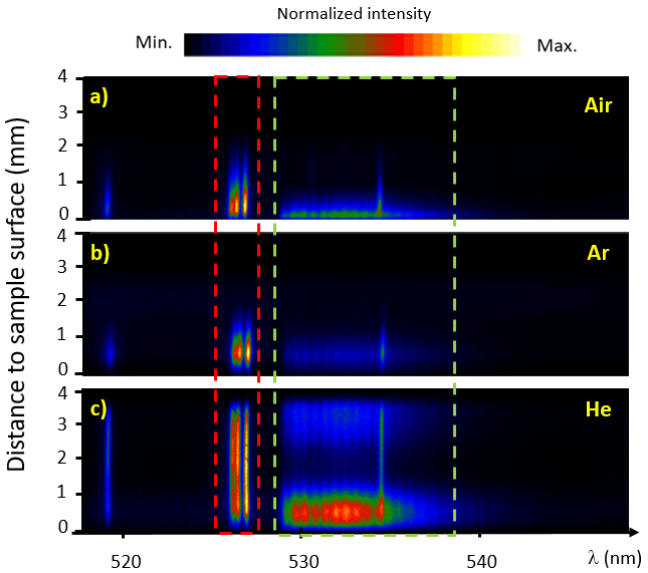

Figure 2. Spectral images taken at a delay time of 5 μs for the CaF_2 sample applying air (a), Ar (b) or He (c) flow. The red dashed contour indicates the atomic Ca emission while the green indicates the molecular CaF emission.

To carefully study the areas of emission predominance, as well as their temporal evolution, both atomic and molecular emission were integrated for each plasma height and at each spectral image acquired at the different delay times. Figure 3 shows the results obtained for some selected delay times. Results in air (Fig. 3(a) and 3(b)) show the already known behavior [27], with the molecular radiation, especially the most intense emission region, restricted to the lower part of the plasma. The atomic emission presents broader distributions with their respective maxima located at a height of around 0.5 mm but with a slight dependence with delay time, first moving upwards and then downwards.

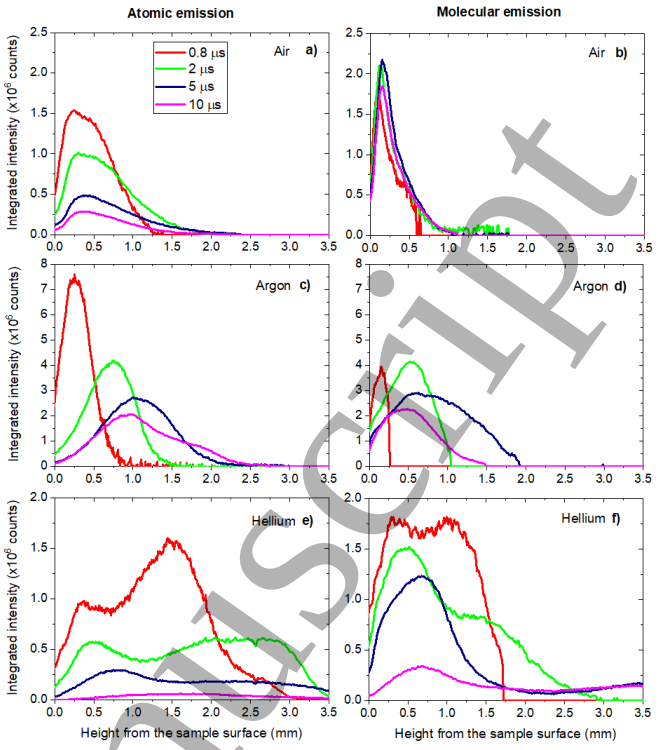

Figure 3. Integrated intensity of the atomic Ca emission (a,c,e) and molecular CaF emission (b,d,f) from the vertical plasma axis as a function of the height, for air (a-b), Ar (c-d) or He (e-f) flow, respectively. As shown in the legend, several distributions acquired between 0.8 and 10 μs are displayed.

In the case of experiments carried out flowing Ar (Figures 3c and 3d), a more pronounced expansion of the plasma was observed. A clear shift of the maximum emission intensity position was obtained for both atomic and molecular radiation up to 5 μs of delay. Specifically, at this delay time the atomic and molecular radiation reach their maximum at a height of 1 mm and 0.75 mm above the sample surface, respectively. From this moment on, both emissions contract again, showing that both radiations move together as the plasma evolves. Although the positions of the maxima of atomic emission are slightly above those of the molecular radiation, the joint motion of both radiations makes it difficult to spatially separate their mutual interferences as clearly as in the case of air flow.

When the plasma is generated under the He flow, there is a pronounced expansion of the emission even at very short delay times, as can be seen in Figures 3(e) and 3(f). It is worth noting the different appearance of the distributions in He, since most of the atomic and molecular curves present profiles with two local maxima. The maximum further away from the surface seems to decrease more rapidly with the delay time, but at the same time, it seems to expand towards greater distances widening the region in which emission occurs. Moreover, as in the cases studied in air and argon, there is always appreciable molecular emission at positions close to the

sample surface. A different emission expansion when generating the plasma in Ar- or He-enriched atmospheres was also reported in previous studies [28,29], and it was related to changes in the heat transfer processes. In order to explain the significative emission expansion for the He case, both the higher thermal conductivity and the lower density of this gas compared to air and Ar should be taken into account. On the one hand, higher thermal conductivity may cause a more efficient energy transfer at the upper boundary region of the plasma plume, which expands upwards, as it was previously reported [28]. On the other, once the laser pulse irradiates the sample, the plasma expansion pushes the surrounding atmosphere outwards. Therefore, a lighter gas environment like He promotes a faster and higher plasma expansion in comparison with heavier gases as air or Ar.

As can be seen in Figure 4, there are also noticeable changes in the total emission intensity according to the flowing gas. In particular, there is a clear increase in both atomic and molecular signals when blowing Ar or He. To evaluate this enhancement, the recorded intensity was summed over all rows of the CCD for both atomic and molecular signals for each spectral image obtained at the different delay times under study. Figure 4 shows the temporal evolution of the total emission, both atomic and molecular, for the three different gas atmospheres.

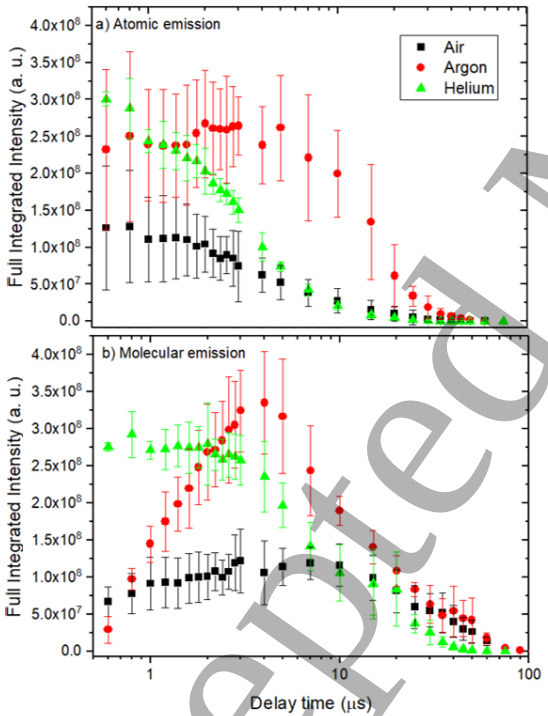

Figure 4. Temporal evolution of the full integrated intensity for (a) atomic Ca and (b) molecular CaF emission. Note logarithmic x-axis scale set for ease of visualization.

Regarding the atomic radiation, the Ca I intensity emitted by plasmas created in air or He atmosphere decreases with time from the first considered delay, with a small gradient at short times in air and with a steeper slope in He. Conversely, the atomic emission from the plasma created in Ar remains constant for the first seven microseconds. If this result is compared with Figure 3(c), we observe that the total intensity remains constant due to the broadening of the spatial distribution, but with much lower maximum intensity. The molecular emission decay is slower than the atomic one in the three atmospheres but with significant differences among them. CaF emission under He flow presents a plateau before it starts decreasing at around 3 μs, while in Ar the emission experiences a fast and pronounced increase up to 5 μs. In air, the emission gradually increases during the first 10 μs. It should be noted that, for both atomic and molecular radiation intensity, the decay in He is the fastest. All these results indicate that under He the plasma evolution is faster, which may be due to the different cooling mechanisms occurring in the plasma. As proposed in [28], it is possible that the plasma in He cools down due to its higher spatial propagation. Furthermore, the use of blown He or Ar in the plasma surroundings involves an increase in both atomic and molecular signal with respect to the results obtained for air, especially for delay times of less than 15 μs.

3.2 Nebulization on a Ca-free model sample

In the nebulization experiments carried out on a PTFE sample, the formation of the CaF molecule involves the recombination of native F species from the solid sample and Ca atoms that are provided by the nebulized aerosol. Due to the continuous operation of the nebulizer, the surface of the sample is covered by droplets at the time of ablation, which is enough to have a noticeable effect on the ablation rate, as shown in a previous work [25]. Therefore, Ca is added both at the very time of ablation as well as throughout the plasma lifetime.

Figure 5 shows the emission in the 533 nm-centered region at three representative delay times, as well as the spectra obtained at different distances (192, 960 and 1920 μm) from the sample surface at a given delay time. The time evolution clearly shows the predominance of atomic Ca I emission that eventually is overshadowed by the emission from CaF molecules. This is in agreement with typical LIP behaviour, but we can note that the earliest delay time shown on Figure 5 exhibits lower continuum emission, as well as an increased presence of molecular adiation with respect to the atomic signal in comparison to CaF_2 powder ablation in absence of nebulization but otherwise analogous experimental conditions [27]. The lower continuum emission suggests lower electron density values in the plasma when nebulization is taking place. It's also worth noting that the expansion of the emission along the vertical axis approximately duplicates that seen on the aforementioned study, an effect that was already observed in previous imaging experiments comparing the plasma plume with and without nebulization for a model Cu sample [25].

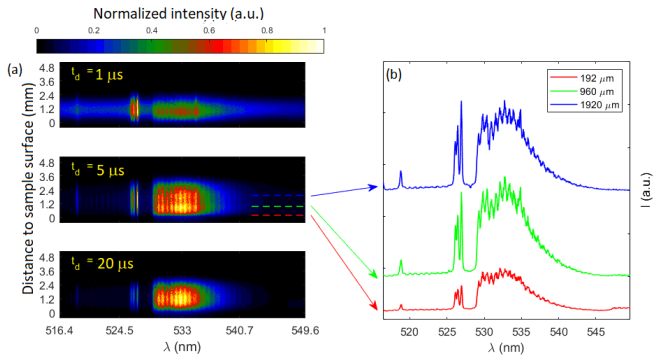

Figure 5. (a) Spectral images of Ca I and CaF emission at different delays and (b) examples of spectra observed at different heights.

The spectra at different heights show that molecular emission predominates at the lower region of the plasma, where the molecular band slightly surpasses the intensity of the Ca I multiplet; at around 547.3 nm, it is also possible to clearly see emission from the green system of CaO (which is interfered by CaOH from 553.8 nm on [33]). Despite an increase of the overall intensity of the CaF molecular emission at higher regions, CaO is not visible further away from the sample. At the highest position shown, Ca I lines show greater intensity than CaF.

In order to obtain more information about CaO emission, a second spectral window was considered. The diffraction grating was centred at 560 nm, collecting the emission from CaO+CaOH between 546.0 and 557.3 nm as well as from a multiplet of Ca I lines with wavelengths between 557.7 to 560.5 nm. Figure 6 shows the spectral images at three delay times, as well as three spectra acquired at a delay of 5 µs and at different distances from the sample surface. The presence of CaO+CaOH is again seen only at the lowest region.

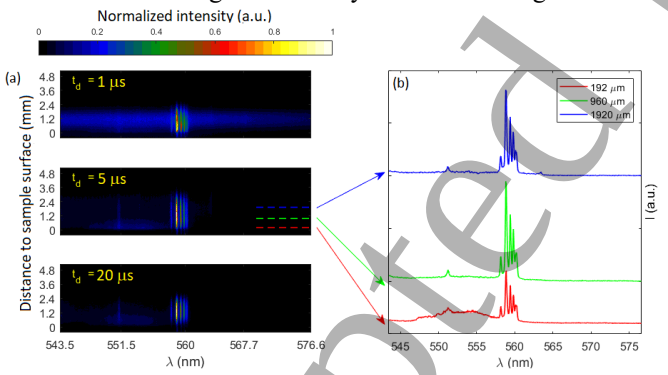

Figure 6. (a) Spectral images of CaO+CaOH and Ca I emission at different delays and (b) Examples of spectra observed at different heights

To find out the behaviour of different plasma species with respect to time and distance to the sample, their respective emission in selected wavelength ranges were obtained. In particular, in the first spectral window, Ca I emission was integrated from 525.0 to 528.1 nm and CaF emission was integrated between 528.1 and 545.0 but excluding a narrow region to avoid Ca I emission at 535.0 nm. In the second spectral window, Ca I was integrated from 557.7 to 560.5 nm, and CaO+CaOH comprised the interval from 546.0 to 557.3 nm also carefully avoiding Ca I emission at 551.3 nm. Prior to signal integration, data treatment involved the sum of 10 pixel rows, so that a single spectrum with a noise reduction was obtained for each 96 µm and then background subtraction was performed.

Figure 7 shows the integrated intensity, normalized at each delay time, with respect to the vertical position along the plasma central axis. It can be pointed out that both atomic Ca I and molecular CaF emission are detected at a broader range of heights than nebulization-less experiments on CaF_2 powder [27], as a result of the increased plasma expansion. The atomic emission (Figure 7(a)) appears more widely distributed; the maximum intensity is found at increasingly higher heights during the plasma expansion in the first 2 µs until it reaches 1.5 mm. The position is found to be practically constant for 10 µs, after which it starts to descend until it cannot longer be detected at around 45 µs.

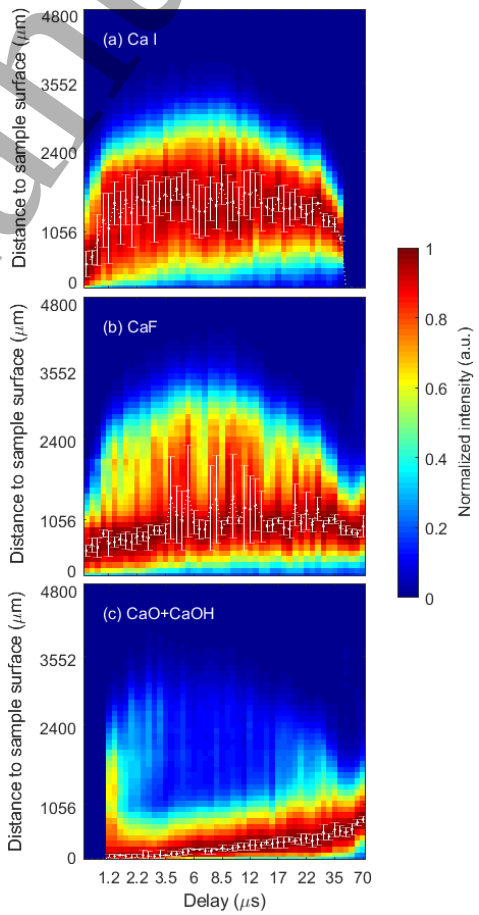

Figure 7. Position of maximum intensity for (a) Ca I multiplet (525-528.1 nm) and molecular emission of (b) CaF and (c) CaO+CaOH green systems.

Molecular emission from CaF (Figure 7(b)) tends to present maximum intensity in a region restricted to the lower heights

of the plasma, but the variability is significant. Instabilities in plume shape due to nebulization are likely to be responsible [25]. It is interesting to note that neither Ca I or CaO+CaOH (Figure 7(c)) seem to present such meaningful instabilities. Maximum CaO+CaOH intensity remains strictly confined to the lower regions, moving upwards very slowly until it barely reaches 1 mm. A substantial difference of the CaF emission behaviour with respect to regular ns-LIBS experiments is the absence of a rapid expansion and upwards displacement towards higher regions at long (>45 μs) delays, something that was consistently observed in absence of nebulization with powder CaF_2 samples [27].

As it is shown in Figure 8, there is a clear separation between Ca I and molecular CaF maximum emission, particularly during the 1.2-3.5 μs delay range at which molecular emission doesn't show high instabilities and the gap between maximum intensities is nearly 1 mm. CaO+CaOH radiation remains at lower positions than the previous species. This is in fact seen in Figure 6.b., where the emission starting at 547 nm can only be seen in the lowest height spectrum (192 μm).

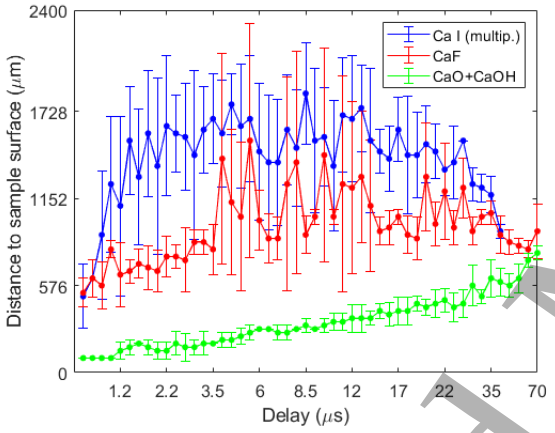

Figure 8. Position of maximum intensity of each species during the plasma evolution

The total intensities, integrated along the vertical axis (i.e. without spatial resolution), as well as normalized to the corresponding gate times are shown in Figure 9. We can see in Figure 9(a) that Ca I decays quickly, following an exponential trend, whereas CaF shows a small increase in intensity until it maximizes at around 3 μs of delay. The following decrease is much slower than that of Ca I. This trend, together with the gap that was pointed out in Figure 8, implies that a delay optimized at around 3 μs could provide good results for analytical purposes using molecular emission detection, since it is most intense in a differentiated spatial region than the atomic signal. On the other hand, the evolution of CaO+CaOH intensity is compared to the Ca I intensity in the same spectral region (multiplet integrated between 557.7 and 560.5 nm). The decay of Ca I is identical to the one shown in Figure 9(a); however, the molecular intensity of CaO+CaOH also decays in a quick exponential fashion, even faster than the atomic emission.

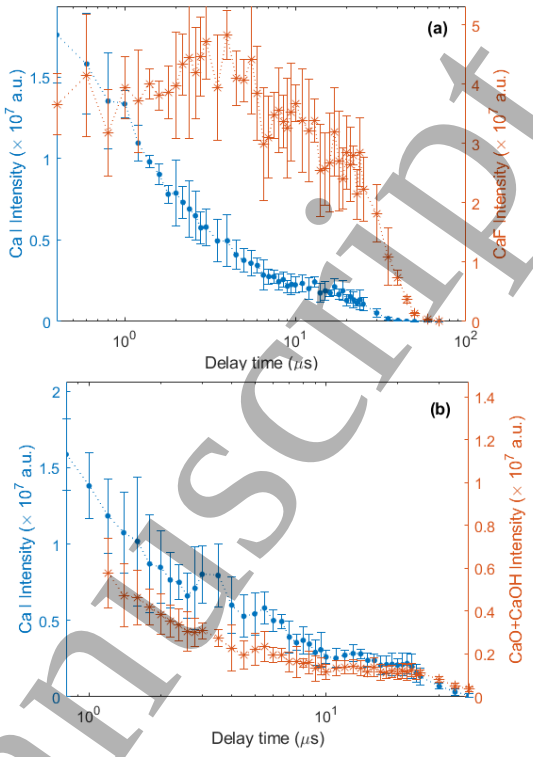

Figure 9. Temporal evolution of spatially integrated intensity for (a) Ca I vs CaF and (b) Ca I vs CaO+CaOH. Note logarithmic scale of the temporal axis.

In order to gain further knowledge about the differences in emission produced by the nebulization itself, two analytical signals belonging to the PTFE sample were chosen: atomic F I (a single integration of three lines at 683.43, 685.60 and 687.02 nm) and molecular C_2 through the Swan system, $A^3\Pi_g$-$X'^3\Pi_u$, emission (integrated in the 462.03-473.98 nm range with a proper gap to avoid interference from Ca I at 468.53 nm) [33].

Figure 10 shows the results obtained from the spatially-resolved data. First of all, it has to be pointed out that due to the high energy (>14 eV) of the upper levels of the involved F I transitions, the emission for this species can only be detected in the first few microseconds. Emission from C_2 also ends at earlier times than the previous molecular emission measurements. In Figure 10(a) we can observe that, under nebulization, F I presents a slight displacement towards higher regions at the beginning, but that at the earliest stage already appears maximized at a height of 1 mm, higher than the Ca I species that were studied. In absence of nebulization (Figure 10(c)), the position of maximum intensity always appears to be distributed around the 1 mm height.

As shown in Figure 10(e), the position of maximum intensity for F I, which doesn't show significant instabilities even under nebulization, is the same at the initial time windows. A split can be seen afterwards, with varying gap of

300-600 µm. The emission of F I is no longer detected slightly earlier under nebulization.

In the case of the C_2 emission under nebulization, Figure 10(b) shows that a vertical displacement takes place steadily until emission is no longer detected, with maximum intensity appearing at around 1 mm and moving up to a 2.4 mm height. However, when PTFE is ablated without nebulizing (Figure 10(d)), the evolution is remarkably changed at around 3.5 µs, after having followed a similar upward displacement. The maximum intensity remains somewhat stable in the 2 mm height region for 5 µs and then moves downwards until emission cannot be detected, 20 µs later than the nebulized-case (Figure 10(f)).

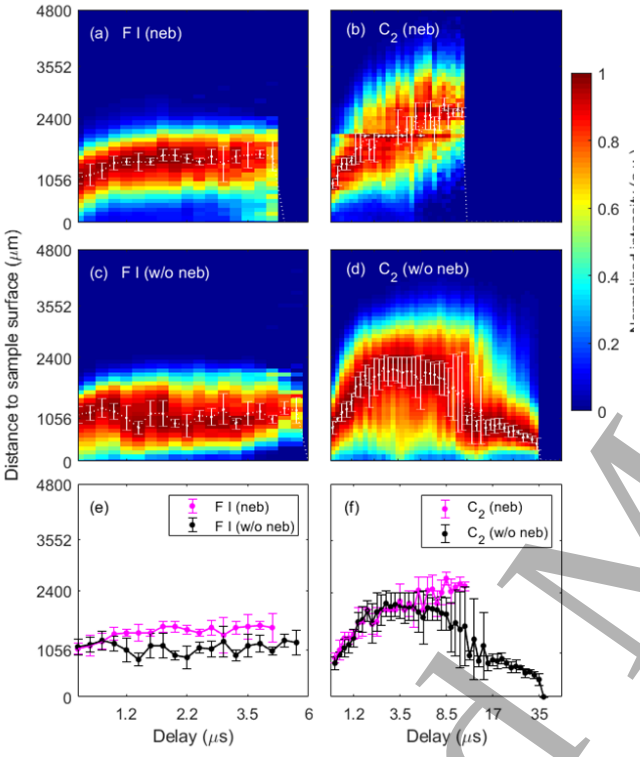

Figure 10. Comparison of two species (F I and C_2) with and without nebulization, showing (a-d) time-normalized, spatially-resolved intensity and (e-f) position of maximum intensity.

The time decays shown in Figure 11 illustrate two main aspects. Firstly, the intensity of fluorine signal (Figure 11(a)) is largely unaffected even though the decay is slightly faster under nebulization. On the other hand, the signal of C_2 (Figure 11(b)) is reduced by a 5x factor under nebulization, as well as having a more pronounced decay. In the case of F I, the emission is detected in a very limited region of the plasma. Given the high excitation energy of the upper levels involved in the detected emission lines, this region could be too hot for molecule formation. In such conditions, the presence or absence of Ca might not be relevant (aside from the vertical displacement of the maximum intensity position due to changes in the plasma plume itself). However, the reason for the strong decrease of C_2 intensity is unclear. If we observe the spatial distribution of the molecular emission in Figure 10(b) and 10(d), it seems that nebulization produces a confinement effect on it; this is, the emission appears more widely distributed along the whole vertical direction when there is no nebulization. Carbon atoms in other regions may be taking part into more energetically-favourable reactions. Since the nebulized solution contains other elements aside from Ca (i.e. O, H and N), other carbon compounds involving them could be formed. However, it cannot be overlooked that the loss of symmetry caused by nebulization could mean that information about other regions of the plasma plume outside of the central vertical axis is needed to interpret these changes.

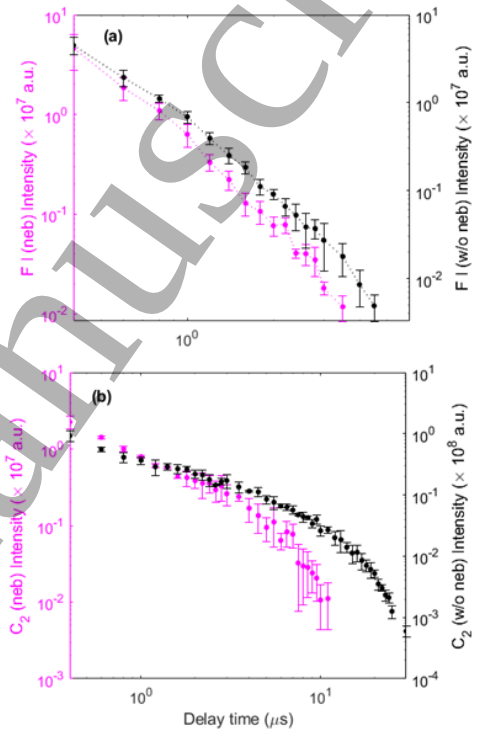

Figure 11. Time evolution of spatially integrated intensity for (a) F I and (b) C_2, both with and without nebulization. Intensities are shown in logarithmic scales to ease visualization.

3.3 CaF formation in femtosecond-laser induced plasmas: a preliminary study

In order to stablish a direct comparison between previous studies carried out with a ns-laser [27], high purity CaF_2 was chosen as a target for the characterization of spatio-temporal distributions of excited atomic (Ca I) and molecular (CaF) species. It has been shown that in ns-LIPs there's a split of the spatial distribution of said emitters, with molecular emission being detected with greater intensity at a lower region of the plasma plume than its atomic counterpart.

Spectral images centered at 533 nm are shown for three temporal delays in Figure 12, in which three spectra at different distances from the sample surface are included to better illustrate emission at different heights. In this case, the molecular emission appears to dominate the spectra at a higher

region than Ca I. The temporal evolution is quite fast and atomic emission disappears from the spectrum at an early stage (<3.5 μs) whereas molecular signal can be detected up to 10 μs after the laser pulse.

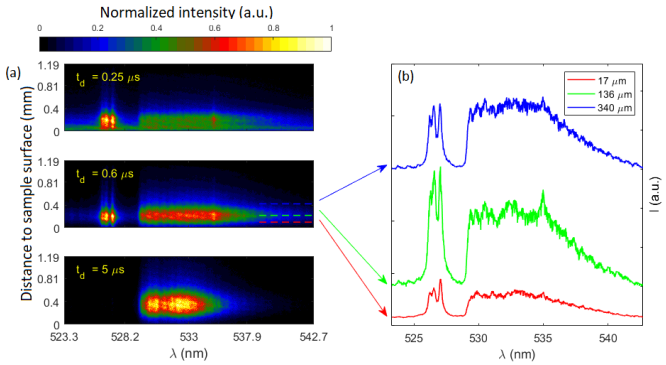

Figure 12. Spectral images in the 523.25-542.70 nm region and examples of spectra at three distances from the sample surface.

The spatiotemporal distribution of intensity for each species, which was obtained analogously to the previous studies, showed a different behaviour than that seen on ns-LIPs, as is shown in Figure 13(a-b). In this case the clear upward/downward displacements at the earliest and latest times of plasma evolution cannot be observed, but instead it is seen that emission moves mostly away from the sample surface. It should be taken into account that the expansion of a femtosecond-laser induced plasma takes place mostly in the vertical direction instead of radially, as it happens with ns-LIPs [14,34], which could translate into the notable upright displacement that is observed.

The location of the maximum intensities of Ca I and CaF don't show a clear, maintained gap in between, as it was the case for nanosecond laser experiments. Instead, Figure 13(c) shows that there is only a limited amount of delay times (0.15 to 0.60 μs) in which molecular emission is maximized at a higher distance from the surface than atomic emission. The difference is about 100 microns.

The spatially-integrated intensity for each species is presented in Figure 14. It shows a clear maximum for CaF at 0.60 μs of delay, as well as a less-acute maximum for Ca I at 0.5 μs. The decay of Ca I is very fast afterwards, and molecular detection could be optimized without the need for spatial resolution, as CaF intensity at 0.7 μs is 72% of the maximum value, whereas at that same delay time Ca I is already at 13% from its maximum. In such circumstances, the potential interference of Ca I is considerably reduced.

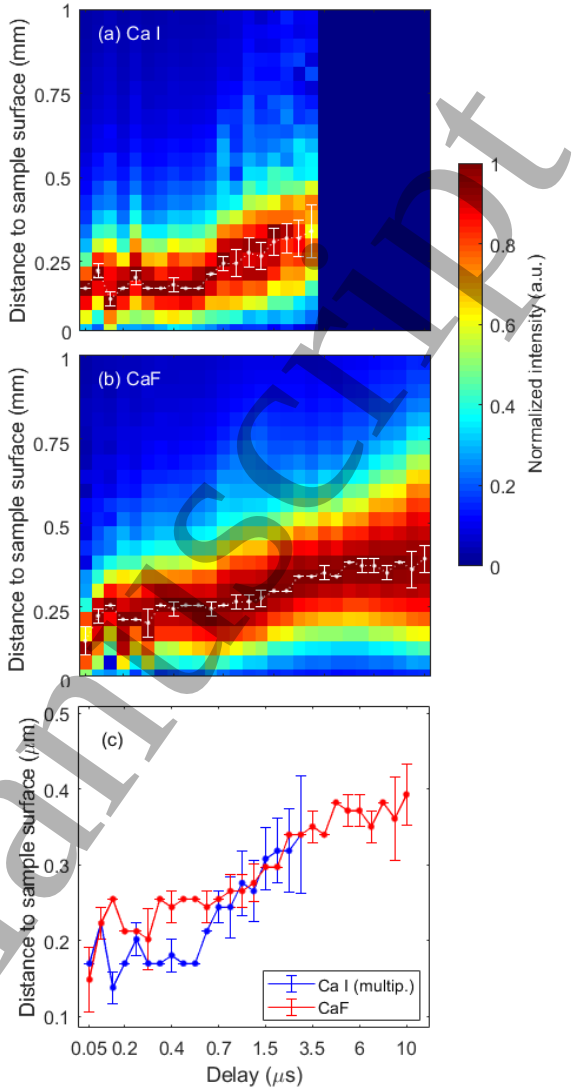

Figure 13. Distribution of the emission signal along the central axis of the plasma corresponding to (a) integrated Ca I emission and (b) integrated CaF emission. (c) Temporal evolution of the position of maximum intensity in each case

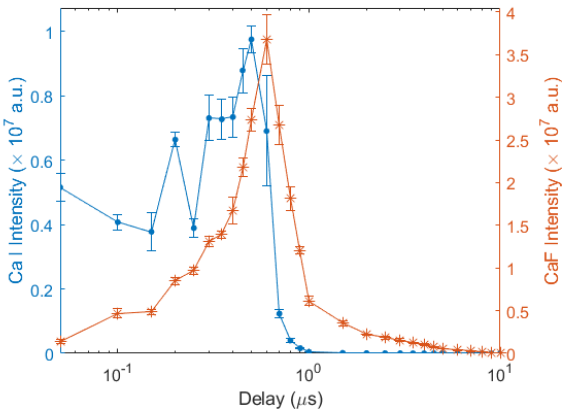

Figure 14. Time evolution of integrated intensity for Ca I and CaF.

It could be noted, however, that powder matrices are not ideal for femtosecond-laser studies. The small size of the laser spot (~60 μm) becomes comparable to powder size (~63-250 μm) and ablation is likely to be affected by irregularities. Additionally, the greater ablation rate could be causing an increase in the ablation of the double-sided tape used to fix the powder. This would introduce Ca into the plasma; in the case of ns ablation, the dissociation of the matrix CaF_2 molecules could mean that the extra amount of Ca is negligible, as most of the signal is being produced by atomized species from the sample, but since femtosecond ablation can preserve native bonds [16] the amount of atomic emission might be being 'artificially' increased. Therefore, further studies focusing on the comparison between ns and fs ablation on CaF_2 will be carried out with pressed powder pellets.

4. Conclusions

In this work the influence of the gas flow in the vicinity of the plasma on the atomic and molecular emission dynamics was evaluated, employing for this purpose both spatial and temporal resolution as a novel feature. It was observed that the air flow applied in the vicinity of the plasma did not greatly influence the propagation of the plume emission, since the plasma lifetime was much shorter than the air flow dynamics.

Conversely, both He and Ar flows cause a larger spatial spread of the emission, especially in He, as well as an increase of the signal, especially with Ar. Such an increase is particularly noticeable for the molecular signal, so in this work it is shown for the first time, to the authors knowledge, that the application of an Ar flow can be evaluated to achieve an improvement of the F detection, when measured by the molecular signal of CaF. On the other hand, the generation of the plasma in He yields large differences in the spatiotemporal distributions of emission with respect to that found in air or Ar. In general, it shows a larger spatial spread and a faster decay due to the lower density and higher thermal conductivity of He. Nevertheless, further research is needed to know the causes of this behaviour.

The studies of spatial distribution of atomic and molecular species under the addition of Ca to a fluorine sample via nebulization showed a similar spatial separation to the one present in CaF-containing samples. Particularly, at early delays there is a 1 mm gap between the maximum emission of each species, with molecular band intensity being consistently maximized at a lower spatial region than its atomic counterpart. Additionally, CaO+CaOH emission remained spatially confined to the bottom of the plume throughout the plasma evolution. Nevertheless the vanishing of atomic emission is not followed by an expansion of the molecular intensity such as it is observed for CaF_2 ablation. It can be concluded that the initial stages of the plasma correspond to an analogous case of CaF-containing samples, having a significant amount Ca-solution being deposited on the sample surface at the moment of ablation. However, the evolution of the plume is known to differ from the non-nebulized case, with higher instabilities that are also seen in the present work, and a notable deviation from a classical cylindrical symmetry model. This could mean that information obtained from the central axis of the plasma might not be entirely representative at longer delays. Hence, plasma diagnostics with suitable filters could be the most logical next step to fully characterize the behaviour of atomic and molecular emission.

Finally, the preliminary study of a fs-laser-induced plasma on a powdered CaF_2 sample showed significant differences with the corresponding ns-laser experiment. As it is expected, fs-LIPs are more short-lived than those induced by nanosecond ablation, and the temporal evolution comprises only up to ten microseconds. In this short amount of time, it is remarkable that molecular emission maximizes further from the sample surface than atomic emission at early delays. However, the gap soon disappears and both are displaced similarly towards upper regions. Additionally, the disappearance of atomic emission is followed by the expansion of molecular emission along the plume as observed with non-nebulized ns-LIPs. Of course, the cylindrical symmetry is overall preserved in this scheme. Regarding analytical potential, the time-gap between maximum integrated atomic and molecular emission suggests that choosing an appropriate acquisition window is the most useful approach for an optimization of molecular detection, rather than the use of a restricted spatial region. Additionally, the plume itself is rather small and so the amount of light that could be collected from a defined region would be very limited.

Acknowledgements

Authors acknowledge financial support from the Spanish Government through the project PID2020-113951GB-I00. Fernández-Menéndez acknowledges financial support via predoctoral grant MINECO BES-2017-080768 and Méndez-López recognizes financial support through predoctoral project PAPI-20-PF-03 (U. of Oviedo) and predoctoral grant PA-21-PF-BP20-059 (Principality of Asturias).

References

[1] Hussain Shah S K, Iqbal J, Ahmada P, Khandaker M U, Haq S, Naeem M, 2020, Laser induced breakdown spectroscopy methods and applications: A comprehensive review, *Radiat. Phys. Chem.* **170** 108666

[2] Senesi G S, Harmon R S, Hark R R, 2021, Field-portable and handheld laser-induced breakdown spectroscopy: Historical review, current status and future prospects *Spectrochim. Acta - Part B At. Spectrosc.* **175** 106013

[3] Liu K, He C, Zhu C, Chen J, Zhan K, Li X, 2021 A review of laser-induced breakdown spectroscopy for coal analysis, *Trends Analyt. Chem.* **143** 116357

[4] Zeng Q, Pan C, Li C, Fei T, Ding X, Du X, Wang Q, 2018, Online monitoring of corrosion behavior in molten metal using laser-induced breakdown spectroscopy, *Spectrochim. Acta - Part B At. Spectrosc.* **142** 68 – 73

[5] Zhang Y, Zhang T, Li H, 2021 Application of laser-induced breakdown spectroscopy (LIBS) in environmental monitoring, *Spectrochim. Acta - Part B At. Spectrosc.* **181** 106218

[6] Velásquez-Ferrín A, Babos D V, Marina-Montes C, Anzano J, 2021, Rapidly growing trends in laser-induced breakdown spectroscopy for food analysis, *Appl. Spectrosc. Rev.* **56** 492-512

[7] Ruan F, Zhang T, Li H, 2019 Laser-induced breakdown spectroscopy in archeological science: a review of its application and future perspectives, *Appl. Spectrosc. Rev.* **54** 573-601

[8] Pérez-Diez S, Fernández-Menéndez L J, Morillas H, Martellone A, De Nigris B, Osanna M, Bordel N, Caruso F, Madariaga J M, Maguregui M, 2021, Elucidation of the Chemical Role of the Pyroclastic Materials on the State of Conservation of Mural Paintings from Pompeii, *Angew. Chem. Int. Ed.* 603028-3036

[9] Busser B, Moncayo S, Coll J L, Sancey L, Motto-Ros V, Elemental imaging using laser-induced breakdown spectroscopy: A new and promising approach for biological and medical applications, *Coord. Chem. Rev.* **358** 70-79

[10] Wiens R C, Blazon-Brown A J, Melikechi N, Frydenvang J, Dehouck S, Clegg S M, Delapp D, .Andersone R B, Cousin A, Maurice S, 2021, Improving ChemCam LIBS long-distance elemental compositions using empirical abundance trends, *Spectrochim. Acta - Part B At. Spectrosc.* **182** 106247

[11] Sigh, J. and Thakur, S. (eds), 2007, *Laser Induced Breakdown Spectroscopy* (Amsterdam, Elsevier B.V.)

[12] Bol'shakov A A, Mao X, Gonzalez J J, Russo R E, 2016, Laser ablation molecular isotopic spectrometry (LAMIS): current state of the art, *J. Anal. At. Spectrom.* 31 119-134

[13] Labutin T, Lednev V, Ilyn A, Popov A, 2016 Femtosecond laser-induced breakdown spectroscopy, *J. Anal. At. Spectrom.* **31** 90-118

[14] Hark R, Musazzi R, Perini P, 2014 Laser-Induced Breakdown Spectroscopy - Theory and Applications (Berlin Heidelberg: Springer)

[15] Carrasco-Garcia I, Vadillo J M, Laserna J J, 2019, Onset of optical emission in femtosecond laser- induced plasmas and its correlation with Surface dynamics monitored by pump–probe time-resolved microscopy, *J. Anal. At. Spectrom.* **34** 2119–2125

[16] Serrano J, Moros J, Laserna J, 2016 Molecular signatures in femtosecond laser-induced plasmas: comparison with naonsecond laser ablation, *Phys. Chem. Chem. Phys.,* **18** 2398-2408

[17] Rao E N, Mathi P, Kalam S A, Sreedhar S, Singh A K, Jagatapc B N, Rao S V, 2016, Femtosecond and nanosecond LIBS studies of nitroimidazoles: correlation between molecular structure and LIBS data, *J. Anal. At. Spectrom.* **31** 737-750

[18] De Giacomo A, Hermann J, 2017, Laser-induced plasma emission: from atomic to molecular spectra, *J. Phys. D Appl. Phys.* **50** 183002

[19] Cremers D A, Radziemski L J, 1983 Detection of chlorine and fluorine in air by laser-induced breakdown spectrometry, *Anal. Chem.* **55** 1252–1256

[20] Tran M, Sun Q, Smith B W, Winefordner J D, 2001, Determination of F, cl, and Br in solid organic compounds by laser-induced plasma spectroscopy, *Appl. Spectrosc.* **55** 739–744

[21] St-Onge L, Kwong E, Sabsabi M, Vadas E, 2002 Quantitative analysis of pharmaceutical products by laser-induced breakdown spectroscopy, *Spectrochim. Acta - Part B At. Spectrosc.* **57** 1131-1140

[22] Gaft M, Nagli L,.Eliezer N, Groisman Y, Forni O, 2014 Elemental analysis of halogens using molecular emission by laser-induced breakdown spectroscopy in air, *Spectrochim. Acta - Part B At. Spectrosc.* **98** 39–47

[23] Alvarez-Llamas C, Pisonero J, Bordel N, 2016, Quantification of fluorine traces in solid samples using CaF molecular emission bands in atmospheric air Laser-Induced Breakdown Spectroscopy, *Spectrochim. Acta - Part B At. Spectrosc.* **123** 157–162

[24] Alvarez-Llamas C, Pisonero J, Bordel N, 2017, A novel approach for quantitative LIBS fluorine analysis using CaF emission in calcium-free samples, *J. Anal. At. Spectrom.* **32** 162-166

[25] Mendez-Lopez C, Alvarez-Garcia R, Alvarez-Llamas C, Fernandez-Menendez L J, Gonzalez-Gago C, Pisonero J, Bordel N, 2020, Laser induced plasmas at different nebulization conditions: Spatio-temporal distribution of emission signals and excitation temperatures, *Spectrochim. Acta - Part B At. Spectrosc.* **170** 105906

[26] Grégoire S, Motto-Ros V, Ma Q L, Lei W Q, Wang X C, Pelascini F, Surma F, Detalle V, Yu J, 2012, Correlation between native bonds in a polymeric material and molecular emissions from the laser-induced plasma observed with space and time resolved imaging, *Trends Analyt. Chem.* **129** 31-37

[27] Fernandez-Menendez L J, Mendez-Lopez C, Alvarez-Llamas C, Gonzalez-Gago C, Pisonero J, Bordel N, 2020 Spatio-temporal distribution of atomic and molecular excited species in Laser-Induced Breakdown Spectroscopy: Potential implications on the determination of halogens, *Spectrochim. Acta - Part B At. Spectrosc.* **168** 105848

[28] Zhang D, Ma X, Wang S, Zhu X, 2015 Influence of ambient gas on laser-induced breakdown spectroscopy of uranium metal, *Plasma Sci. Technol.* **17** 971-974

[29] Aguilera J, Aragón C, 1999 A comparison of the temperatures and electron densities of laser-produced plasmas obtained in air, argon and helium at atmospheric pressure, *Appl. Phys. A*, **69** 475-478

[30] Rajavelu H, Vasa N J, Seshadri S, 2021 LIBS technique combined with blow gas and vacuum suction to remove particle cloud and enhance emission intensity during characterization of powder samples. *Spectrochim. Acta - Part B: At. Spectrosc.,* **181** 106215

[31] Dawood M S, Hamdan A, Margot J, 2015, Influence of surrounding gas, composition and pressure on plasma plume dynamics of nanosecond pulsed laser-induced aluminum plasmas, *AIP Adv.* **5** 107143

[32] Kramida, A., Ralchenko, Yu., Reader, J. and NIST ASD Team (2021). NIST Atomic Spectra Database (version 5.9), [Online]. Available: https://physics.nist.gov/asd [Fri Feb 18 2022]. National Institute of Standards and Technology, Gaithersburg, MD

[33] Pearse, R.W.B. and Gaydon, A.G., 1984, *The Identification of Molecular Spectra* (Chapman and Hall).

[34] Verhoff B, Harilal S, Freeman J, Diwakar P, Hassanein A, 2012, Dyanmics of femto- and nanosecond laser ablation plumes

investigated using optical emission spectroscopy, *J. Appl. Phys.* **112** 093303